Strategies for Improving Detection of Magnetic Nanoparticles in Magnetomotive Ultrasound

Sophia Stickel

2026

LUND
UNIVERSITY

Master's Thesis in Biomedical Engineering

Faculty of Engineering LTH
Department of Biomedical Engineering

Supervisors: Jules Reniaud, Maria Evertsson, Tomas Jansson

Abstract

Magnetomotive ultrasound (MMUS) is a developing imaging modality using magnetic nanoparticles (MNPs) as contrast agent. MNPs are accumulated at a tissue target and set in motion by a time-varying magnetic field. The resulting displacement spreads to surrounding tissue and is detected with ultrasound. The objective of this modality is to transition medical ultrasound from structural to molecular specific imaging, with application potential for cancer cell detection and drug administration. An existing MNP detection method is based on quadrature demodulation and phase gating. However, the detection limit remains constrained by the method's sensitivity to noise. Additionally, cardiorespiratory rhythms increase the risk of spectral leakage in the detection of fixed frequency magnetic excitation commonly used for MMUS. To overcome these limitations, I implemented three strategies to improve the detection of MNPs in MMUS and evaluated their efficiency with a contrast-to-noise ratio (CNR) on tissue-mimicking phantoms with descending MNP concentrations. The first strategy was frequency modulated magnetic excitation signals, specifically linear bidirectional chirp signals generated with a rotating permanent magnet. Secondly, I developed a matched filter algorithm that correlates phase oscillation in ultrasound radio frequency (RF) data with a magnetic force reference. The resulting normalized correlation was employed as a probability mask, where each pixel value represents the likelihood of MNP presence, used for weighting the results of the previous detection method. The third strategy was implementation of thresholding for segmentation and morphological filtering to suppress noise and refine object boundaries on the mask. The chirp excitation signals did not substantially improve the visibility of accumulated MNP regions compared to fixed frequency excitation signals. Thus, the use of these signals is not justified. When the previous detection method was combined with the probability mask from the matched filter, the CNR increased by 6.6 dB for 0.5 mg/ml of MNPs, 7.6 dB for 0.3 mg/ml of MNPs and 13.2 dB for 0.1 mg/ml of MNPs. Segmentation and morphology further improved the CNR with 1.6 dB for 0.5 mg/ml of MNPs, 1.7 dB for 0.3 mg/ml of MNPs and 16 dB for 0.1 mg/ml of MNPs. These results demonstrate that the matched filter algorithm and image processing enhance noise suppression and spatial specificity in MMUS, likely allowing detection of lower MNP concentrations.

Populärvetenskaplig sammanfattning

Så hittas cancer med magneter och ultraljud

Genom att kombinera ultraljud med magnetiskt kontrastmedel kan man hitta cancerceller som tidigare varit osynliga. Detta banar vägen för billigare cancerdiagnostik utan strålning. En algoritm som utvecklats i detta arbete gör metoden ännu mer pricksäker.

Frisk vävnad och tidiga cellförändringar ser nästan identiska ut med vanligt ultraljud. Att försöka skilja dem åt är därför som att leta efter en nål i en höstack. Jag har utvecklat en algoritm för magnetomotoriskt ultraljud som kan måla upp gränsen mellan friskt och sjukt med högre noggrannhet än tidigare metoder. Denna teknik öppnar dörren för cancerdiagnostik som är strålningsfri, billigare och mer tillgänglig än dagens metoder.

Idag används ofta dyra tekniker som MR och PET för att hitta specifika cancerceller. Ultraljud hade varit ett perfekt komplement till dessa om det inte vore för den dåliga kontrasten. Lösningen kan vara magnetiska järnpartiklar som kontrastmedel. Dessa små partiklar injiceras i kroppen och söker upp cancerceller. Genom att sedan skaka om dem med ett starkt magnetfält får man omgivande vävnad att vibrera. Det är dessa vävnadsvibrationer som upptäcks med ultraljudet i tekniken som kallas för magnetomotoriskt ultraljud.

Min nya algoritm fungerar som ett avancerat filter. Genom att matcha vävnadens rörelse med magnetfältets svängningar kan algoritmen rensa bort brus och fokusera helt på vibrationerna från järnpartiklarna. Det gör att även mycket små mängder kontrastmedel syns tydligt. Detta är viktigt för att tekniken ska bli så känslig som möjligt för diagnostik.

För att testa algoritmen gjordes experiment på vävnadsliknande fantomer, tänk som ett bröstimplantat med en konstgjord tumör i. En roterande magnet skapade magnetfältet som fick järnpartiklarna i ”tumören” att vibrera samtidigt som en ultraljudsgivare tog bilder. Hypotesen var att om magneten snurrade med varierande rotationsfrekvenser skulle vibrationerna vara lättare att hitta. Resultatet visade oväntat nog att det fungerar lika bra med en konstant frekvens. Däremot ger den nya algoritmen noggrannare detektion, bara genom att analysera samma data på ett annat sätt.

Use of AI

Generative AI has been utilized in two main areas during this thesis project. The first objective was to assist with the coding in MatLab, and the second was to reformulate heavy sentences for the report. The primary AI model used was Gemini Pro. All suggestions were verified and adjusted to ensure academic accuracy.

Acknowledgements

I want to thank my supervisors, Jules Reniaud, Maria Evertsson and Tomas Jansson, for giving me the opportunity to work on this project. You have all been so generous with your time, ideas, knowledge, guidance and encouragement throughout this process. For that I am truly grateful, and I will never forget it. Thank you Magnus Cinthio for being my examiner and thank you to the entire ultrasound group for being so welcoming and helpful.

To my family and friends, thank you for believing that I can become whoever I want and for cheering me on. Thank you Mamma, Pappa, Mormor, Morfar, Oma and Opa for the choices you make and made in your lives that give me so much freedom in mine.

Contents

1 Introduction

Imaging is one of the strongest and most critical diagnostic tools in modern medicine. By tracking structural and physiological changes in the body, physicians can make decisions about diseases and treatment courses. This is invaluable for the diagnosis of various types of cancer (Hussain et al. 2022). However, the goal is to diagnose cancer in earlier stages, before a visible tumor forms. To achieve this, current imaging developments are focused on molecular specificity. Molecular imaging involves labeling specific cells to make them visible. This allows for tracking of individual cell types, instead of focusing on anatomy and structure. Successful molecular imaging can reveal the cause of a disease before anatomical changes occur. One such application is the localization of cancer metastases (Hood et al. 2004).

Imaging modalities that allow molecular specificity include magnetic resonance imaging (MRI), positron emission tomography (PET), single photon emission computed tomography (SPECT) and optical methods. The main drawbacks of these techniques are the high cost of MRI, the ionizing radiation in PET and SPECT, and the shallow penetration depth of optical methods (Sjöstrand et al. 2020). An alternative, complementary modality could be ultrasound. Although ultrasound is less suitable for whole-body screening to detect new cancer occurrences, it could be valuable to localize known tumors or regional metastases. It is a widely accessible and inexpensive modality that is free of ionizing radiation and capable of reaching deeper targets (Hoskins et al. 2019). However, the contrast between early stage cancer and healthy tissue is inadequate for distinction with conventional ultrasound. Instead, contrast agents that can be coated with antibodies or other types of proteins are needed to target specific cells. Commercial ultrasound contrast agents have mainly consisted of micrometer-sized bubbles of air. These bubbles are confined to the vascular system, limiting the cells they can target. As an alternative, superparamagnetic iron oxide nanoparticles (SPIONs) have been proposed as a contrast agent for ultrasound, in a technique called magnetomotive ultrasound (MMUS). These particles could also be coated to target specific cells, and their size allows them to escape the vascular system (Sjöstrand et al. 2020). Another advantage of utilizing SPIONs for MMUS is their established clinical history. As they are already an available contrast agent for MRI, they are accepted for medical use (O'Donnell 2018).

If the magnetic nanoparticles (MNPs) are successfully coated with specific ligands, this could unlock a wide range of application opportunities for MMUS. An example is visualization of drug administration. By functionalizing the particles with chemotherapeutic drugs, a local treatment called magnetic drug targeting can deliver chemotherapy directly to cancer cells. Indirectly, MNPs would serve as the contrast agent for MMUS, allowing visualization of drug dosing. This is vital to optimize drug delivery to the tumor and achieve a successful treatment. The successful use of MMUS for this application could hopefully complement the use of MRI (Fink et al. 2017). Another proposed application for MMUS is as an intraoperative guide. By accumulating MNPs at a metastasized lymph node, the technique has been shown to act as a complement to standard PET or MRI during lymph node removal. The implementation of MMUS would limit radiation exposure for surgical staff (Evertsson et al. 2017).

However, the nanometer-size of the MNPs limits their backscattering echo, making it impossible to detect them directly with ultrasound. Instead, MMUS exploits the magnetic properties of MNPs. When the contrast agent has accumulated at the tissue target, a strong time varying magnetic field causes displacement of the MNPs. The displacement spreads to surrounding tissue that, in turn, vibrates with the same frequency as the MNPs (Sjöstrand et al. 2020) (Fink et al. 2017). To detect tissue displacement, subsequent conventional ultrasound images are taken to capture tissue displacement in the time domain.

Fixed frequency sinusoidal magnetic excitation signals are commonly used for MMUS applications (Fink et al. 2016). A developed detection method for MNPs based on a fixed frequency oscillation is the phase tracking algorithm described by Evertsson et al. (2013). The method quantitatively assesses tissue displacement at a specific frequency based on phase gating and quadrature detection. However, the detection limit of MNPs remains constrained by the method's sensitivity to noise. Additionally, biological rhythms like heartbeats and respiration increase the risk of spectral leakage in the detection of fixed frequency magnetic excitation commonly used for MMUS. To overcome these limitations, I propose frequency modulated excitation signals to increase noise suppression and to lower the detection limit. Furthermore, I aim to investigate how matched filtering and image processing can enhance noise suppression and spatial specificity in MMUS imaging.

To evaluate the detection limit of the matched filter algorithm and the frequency modulated excitation signals, I demonstrate their performance using tissue-mimicking phantoms of decreasing MNP concentration. Specifically, I quantify the improvements in noise suppression using the contrast-to-noise ratio (CNR) and compare the matched filter algorithm with the previous phase tracking algorithm to highlight the gained specificity.

2 Background

2.1 Magnetomotive force

The magnetomotive force is the force acting on the MNPs when subject to a magnetic field. With a time-varying magnetic field $B(t)$, the magnetic gradient force acting in the axial direction on a particle can be approximated by Equation (1),

$$F_y = \frac{V\chi}{\mu_0} B(t) \frac{\partial B(t)}{\partial y} \tag{1}$$

where V is the volume of the particle, χ is the magnetic susceptibility of the particle and μ_0 is the magnetic permeability of vacuum (Sjöstrand et al. 2018). If the magnetic field is a fixed frequency sinusoid, it is described by Equation (2),

$$B(t) = B_0 sin(2\pi f t) \tag{2}$$

where B_0 is the amplitude of the magnetic excitation, f is the frequency and t is time. The magnetic gradient force on the particle will be proportional to the magnetic field multiplied by the derivative of the magnetic field, as described in Equation (1). The proportionality is described in Equation (3).

$$F_y \propto B(t) \frac{\partial B(t)}{\partial y} \propto B_0 \frac{\partial B_0}{\partial y} sin^2(2\pi f t) \tag{3}$$

The trigonometric identity can be used to further simplify the expression, see Equation (4).

$$F_y \propto B_0 \frac{\partial B_0}{2\partial y} (1 - cos(4\pi f t)) \tag{4}$$

The result in Equation (4) shows that the magnetic gradient force on the particle will have twice the frequency as the magnetic field. Additionally, the magnetic force is proportional to the magnetic field squared, given by comparing Equation (2) and Equation (3). This means that if the magnetic field is measured, a proportional reference for the magnetic gradient force can be calculated by squaring the magnetic field. These proportionalities also hold for a frequency modulated magnetic field but are presented for the fixed frequency case to maintain clarity and simplicity.

2.2 Previous work

Different magnetic excitation signals have been used in MMUS. Fixed frequency sinusoidal signals, pulsed signals, chirped signals, where the frequency speeds up over time, and Barker code sequenced signals are some examples. A summary of previous work on frequency modulated excitation signals in MMUS is provided below.

Frequency modulated excitation signals are characterized by their instantaneous frequency, which varies over time. Fink et al. (2016) studied the detection of MNPs using a linear up-chirp signal in MMUS. This signal has a lower initial frequency than peak frequency and accelerates linearly over time. Fink et al. (2016) presented an algorithm for detection based on the fractional Fourier transform which allowed detection of MNPs in a tissue-mimicking phantom. Fink et al. (2017) investigated a 4-bit Barker coded sequence instead. This frequency modulated signal switched between two different frequencies in a Barker sequence with two possible states, -1 and +1. In their implementation, the -1 state corresponded to one frequency while the +1 state corresponded to another frequency. The signal was specifically evaluated when exposed to noise up to 5 Hz, applied to mimic biological functions. Fink et al. (2017) compared the Barker sequence performance to that of a fixed frequency signal and found that the coded excitation resulted in a more specific spatial confinement of the magnetic region of a tissue-mimicking phantom than the fixed frequency signal. Gu et al. (2025) compared a single-pulse signal, a linear up-chirp excitation and a 13-bit Barker coded sequence. In their implementation, opposite states in the Barker code corresponded to opposite phases of the same frequency. The results of Gu et al. (2025) included a detectable concentration of 10 mg/ml MNPs for both coded signals compared to 100 mg/ml for the single-pulse signal, with an improved CNR. However, their study did not include a comparison with a continuous fixed frequency sinusoidal signal. All mentioned previous studies on frequency modulated excitation signals have utilized an electromagnet to drive the MNP displacement. In this contribution, I use a rotating permanent magnet to induce the time-varying magnetic field on the MNPs.

2.3 Phase tracking algorithm

The phase tracking algorithm is an MNP detection method for MMUS developed by Evertsson et al. (2013). The method calculates tissue dis-

placement at one specific frequency by mixing the phase of the received ultrasound radio frequency (RF) data for each pixel with a reference sinusoid at the magnetic excitation frequency (in-phase component) and its 90°shifted counterpart (quadrature component). This step filters out all other frequency components. The amplitude and phase of the quadrature detected sequence are calculated. The amplitude is converted to displacement magnitude for the tissue in each pixel and the phase is used for gating. The gating is a manual decision by the operator to filter out pixels that move out of phase with the MNP region. The resulting output is a displacement detection map for the ultrasound image.

3 Method

3.1 Phantom preparation

Phantoms are tissue-mimicking objects that are used for evaluating imaging techniques on inanimate objects before moving on to animal or human testing. Using ultrasound phantoms is often preferred as a starting point because of its economical and ethical advantages (Mousavi et al. 2025).

3.1.1 Oil-based bulk material

Phantoms were created to resemble human fat, with an embedded insert of SPIONs that symbolized a tissue region with accumulated contrast agent. The bulk material of the phantom was 3 wt.% styrene-ethylene-butylene-styrene (SEBS, Kraton G1650 EU, USA), a type of copolymer with plastic or rubber-like properties, mixed with mineral oil (330779, Sigma-Aldrich, Germany). The percentage of SEBS in oil was mimicked from previous studies by Mousavi et al. (2025), to have a Young's modulus (stiffness) that closely relates to human fat. Graphite (282863, Sigma-Aldrich, Germany) at 1 wt.% was used as the scattering material for ultrasound. The insert material was 5 wt.% polyvinyl alcohol (PVA, 341584, Sigma-Aldrich, Germany), 1.5 wt.% graphite for attenuation and descending concentrations of SPIONs (Ocean Nanotech, USA) as contrast agent for MMUS.

The preparation was dimensioned for three separate phantoms. The total weight of the prepared bulk material was 300 g. The preparation began by combining 87.5% (252 g) of the total weight of mineral oil (288 g) with 9 g of SEBS, resulting in 3 wt.% SEBS. The mixture was heated in an oven (FN 300, Nüve, Turkey) at 120°C for 2 hours. The rest of the mineral oil (36 g) was combined with 3 g of graphite (1 wt.%) and combined with the heated SEBS solution. The two mixtures were stirred with a magnetic stirrer for 5 minutes before being added to three phantom molds. A 5 mm diameter metal rod was inserted into each mold before the SEBS hardened to create a cylindrical hole for the PVA insert. See Figure 1 for a schematic illustration of the phantom mold. The phantoms rested in room temperature for 2 hours before the metal rod was removed.

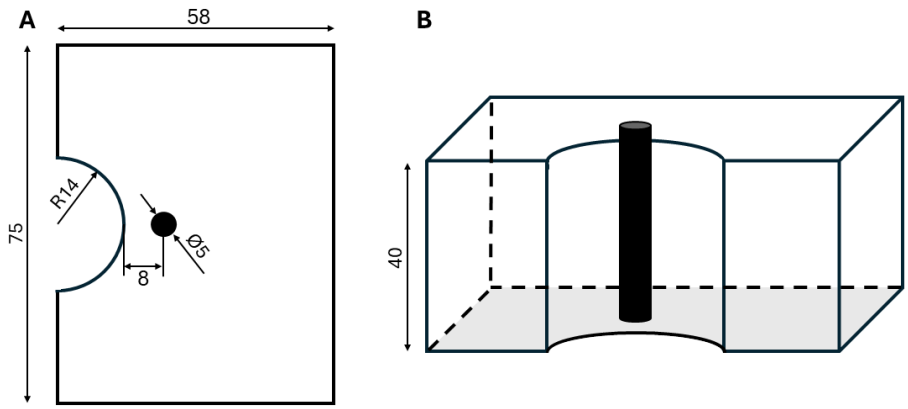

Figure 1. Schematic illustration of the phantom molds from (A) the top and (B) the side. Lengths are in mm. The black 5 mm diameter cylinder is the PVA insert.

The preparation of the inserts began by combining 9.3 ml of Milli-Q water with 0.56 g of PVA. The mixture was heated in the oven at 100°C for 1 hour before adding 0.17 g of graphite. Water was added to compensate for the loss from evaporation. The solution was divided into three parts, each 1.35 g, and MNPs were added to each part at concentrations of 0.5, 0.3 and 0.1 mg/ml. The particles used were SPIONs in water with a diameter of 30 nm (Ocean Nanotech, USA). Extra water had to be added to the lower concentrations to achieve a total weight of 1.5 g for each insert. The final composition of the inserts was 5 wt.% PVA and 1.5 wt.% graphite.

Next, the PVA was poured into the cylindrical hole that the metal rod had left in the SEBS mold. To remove air bubbles, the phantoms were placed in a vacuum pump for 20 minutes at a pressure of approximately -15 inHg. More PVA was added in case there was room in the cavity and another vacuum pump cycle at -15 inHg was employed for 2 minutes. The phantoms were then placed in a freezer. After 18 hours, the phantoms were moved to rest at room temperature for 2 hours before the residual SEBS solution was added to seal the PVA to prevent evaporation. The residual SEBS solution had been heated at 100°C for 30 minutes to melt again. The phantoms had a final rest at room temperature for 2 hours before being ready for the experiments.

3.1.2 Water-based bulk material

A version of phantoms was created in which both the bulk and insert material was polyvinyl alcohol (PVA). The aim of this fabrication was to investigate a water-based bulk material, just as human tissue is, and to evaluate the detection capacity of MMUS in a phantom with identical acoustic properties in the bulk and insert material. In both materials, 5 wt.% PVA (341584, Sigma-Aldrich, Germany) determined the stiffness of the material and 1 wt.% graphite (282863, Sigma-Aldrich, Germany) was used as the scattering material for ultrasound. In the insert material, SPIONs (Ocean Nanotech, USA) were used as contrast agent for MMUS.

The preparation was dimensioned for three separate phantoms, in the molds illustrated in Figure 1. To prepare the bulk material, 282 g of Milli-Q water was mixed with 15 g of PVA. The mixture was heated in an oven (FN 300, Nüve, Turkey) at 100°C for 3.5 hours and stirred every half hour to reach a point where the PVA was melted and transparent. However, this point was never reached. The PVA did not fully dissolve and the solution had to be removed from the oven before all of the water evaporated. After heating, 3 g of graphite was added and stirred into the solution for 5 minutes with a magnetic stirrer. The loss of water was calculated and added accordingly to ensure a final composition of 5 wt.% PVA and 1 wt.% graphite. The mixture was poured into three molds and a 5 mm diameter metal rod was inserted into each mold to create a hole for the insert.

The insert material was created in the same way, with 5 wt.% PVA and 1 wt.% graphite. The total volume prepared for the insert material was 10 g. This mixture was heated in the oven at 100°C for 1 hour. SPIONs in water with a diameter of 20 nm and 30 nm (Ocean Nanotech, USA) were used as contrast agent and mixed into three parts of the PVA solution at 0.5, 0.3 and 0.1 mg/ml. The 0.5 and 0.3 mg/ml solutions had 20 nm particles, while the 0.1 mg/ml had 30 nm particles. The solutions were sucked into three syringes with an inner diameter of 5 mm.

Two freeze-thaw cycles were performed to polymerize the bulk and insert solutions. The molds and syringes were put in the freezer for 18 hours. Then they were placed in the fridge for 8 hours before thawing at room temperature for 20 hours. A new cycle was started by freezing the phantoms for 20 hours before thawing them for 24 hours at room temperature. The syringe tops were cut with a scalpel and the metal rods were removed

from the phantom molds. The magnetic insert was pushed into the hole in the phantom with the syringe before being ready for experiments.

3.2 Experimental setup

An illustration of the experimental setup is shown in Figure 2. The phantom was placed between the rotating permanent magnet and the ultrasound transducer. Images were acquired with the Vevo F2 system (FUJIFILM VisualSonics, Canada) and the linear ultrasound transducer L38. The transducer had a transmission frequency of 7.1 MHz. All images were acquired with a cine-loop of either 200 or 250 frames, with a sample frequency of 50 frames per second. A cine-loop captures a sequence of ultrasound images over time. This means that a 200 frame cine-loop was 4 seconds long and a 250 frame cine-loop was 5 seconds long. 200 frame cine-loops were used for the fixed frequency signals and the 1 second duration chirp signals, while 250 frame cine-loops were used for the 2 second duration chirp signals. The length of the cine-loop was thus adjusted to ensure a whole bidirectional chirp cycle fit in the recording. The gain and focus were adjusted on the ultrasound system for each phantom, specifically to avoid clipping the RF-data collected during image capture. Data were acquired for three cross sections of each phantom.

A rotating permanent magnet generated the time varying magnetic field used to drive displacement of the MNPs. The magnet is shaped like a cylinder, made of neodymium and diametrically magnetized (K&J magnetics, USA), which means that the magnet is magnetized across the diameter, with a pole on opposite curved sides. The outer diameter of the magnet housing is 28 mm. To create a sinusoidal magnetic field acting on a stationary object on one side of the cylinder, the magnet revolved around its own axis, alternating the poles location in relation to the object. To drive the magnet rotation, an EPOS2 motor controller and a motor (DCX 22 S maxon motors, Switzerland) were connected to the magnet. The motor was in turn powered by a 20 V power supply (PSI 8080-60 T, EA Elektro- Automatik GmbH & CO. KG, Germany) and controlled from a computer. The magnet was placed flush to the phantom before being moved 2 mm out, making sure that no part of the magnet was in contact with the phantom to decrease the likelihood of mechanical vibrations from the contact interface. This resulted in a total distance of 1 cm from the magnet edge to the center of the PVA insert.

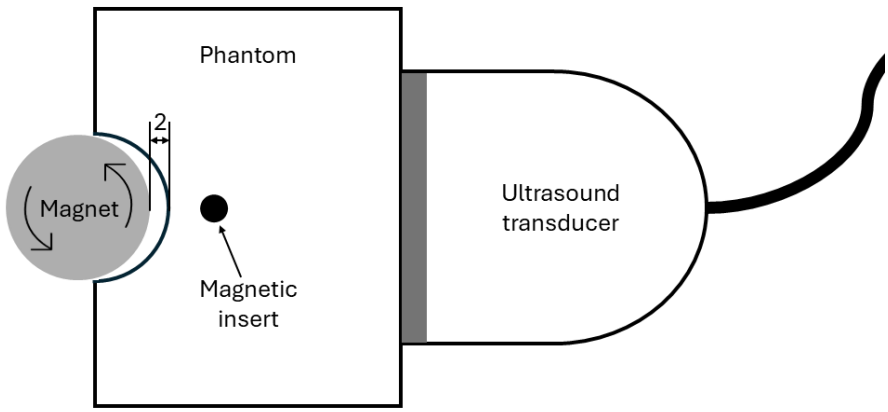

Figure 2. Schematic illustration of the experimental setup. Lengths are in mm.

An image of the experimental setup is shown in Figure 3. The bulk material was black from the graphite, which is why the magnetic insert could not be seen. The mounting of the ultrasound transducer was placed on a separate table from the magnet and its power supply. This was deliberately done to minimize the risk of mechanical vibrations.

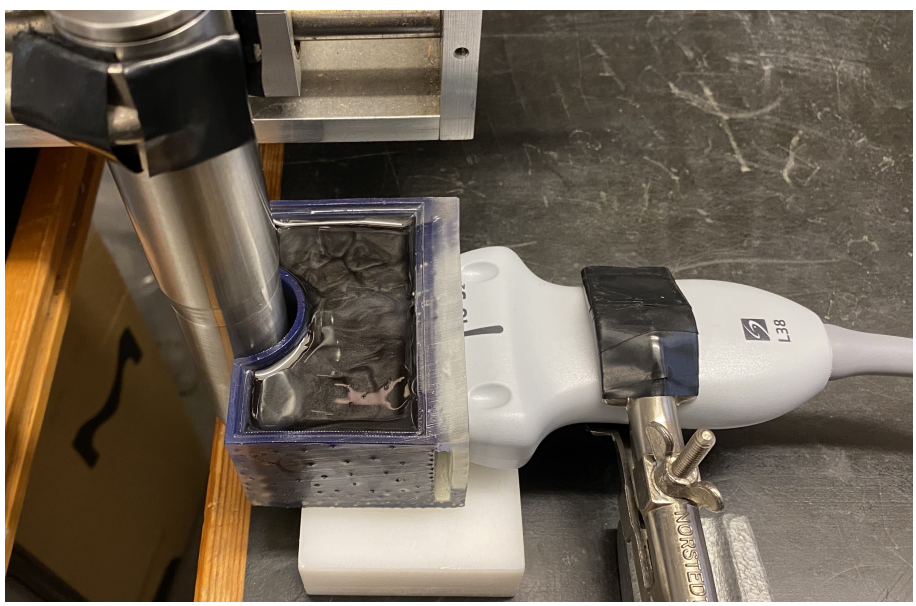

Figure 3. Image of the experimental setup for measurements.

3.3 Frequency modulated magnetic excitation

The frequency modulated magnetic excitation signal used in this contribution was a linear bidirectional chirp. In this model, the instantaneous frequency $f(t)$ varies linearly over time. The rate of this change, or the chirp rate c, is defined in Equation (5),

$$c = \frac{f_p - f_0}{T/2} \tag{5}$$

where f_p is the peak frequency, f_0 is the lowest frequency and T is the total modulation period (Fink et al. 2016). Note that for a bidirectional sweep, the frequency had to change from f_0 to f_p in half the total period ($T/2$). To maintain frequency continuity and ensure that there was no phase jump, the signal for the second half of the period ($T/2 \leq t < T$) had to begin at the frequency value reached at $t = T/2$ and decelerate using a negative chirp rate. This created a periodic sweep where the magnetic field linearly accelerated to its peak frequency and symmetrically returned to its minimum. The resulting magnetic field followed Equation (6) with its instantaneous frequency defined in Equation (7).

$$B(\tau) = B_0 + B_0 \sin\left(2\pi \int_0^{\tau} f(t),\, dt\right) \tag{6}$$

$$f(t) = \begin{cases} f_0 + ct, & 0 \leq t < T/2 \\ f_p - c(t - T/2), & T/2 \leq t < T \end{cases} \tag{7}$$

To create a frequency modulated magnetic excitation, I designed a control system with MatLab (The MathWorks Inc., USA). EPOS2 libraries, including a USB driver and function files (Eugenio 2026), were integrated into the control system. The implemented control system enabled the magnet to rotate both at a fixed frequency and via a frequency modulated signal. Specifically, the system utilized linear bidirectional chirps with adjustable parameters to control modulation duration and peak frequency. The system calculated a velocity vector based on the parameters and continuously updated the motor command. In this way, the signal could change frequency over time.

The evaluated fixed displacement frequency signals were 1.7 Hz, 6.7 Hz and 13.3 Hz. The chirped signals that were evaluated all had the lowest frequency 1.7 Hz and a peak frequency of 3.3 Hz, 6.7 Hz and 13.3 Hz,

respectively. All chirped signals were tested for a duration of 1 second and 2 seconds. The magnetic field frequency was half of the frequency of the MNP oscillations presented here according to Equation (4).

During experiments, I noticed that the motor updates experienced lagging, resulting in longer magnetic chirp durations than expected. This meant that an artificial reference that matched the intended signal would not be sufficient to find the chirped magnetic excitation in the ultrasound data. To combat this issue, a measured reference was obtained with a Three Axis Hall Magnetometer THM1176 (Metrolab Technology SA, Switzerland). Measurements were recorded with the magnetometer probe in direct contact with the permanent magnet at the cross section of the cylinder with maximum magnetization. An example of a measured reference magnetic field signal is presented in Figure 4A. The graph in Figure 4B shows the resulting proportional magnetic force reference acting on the MNPs, which was calculated by squaring the measured magnetic field. This means that the amplitude of the reference force is not accurate since no material specific parameters were included in the calculation. However, it was the timing and frequency of the magnetic force that had significance for detection, which meant that a reference proportional to the magnetic gradient force was sufficient.

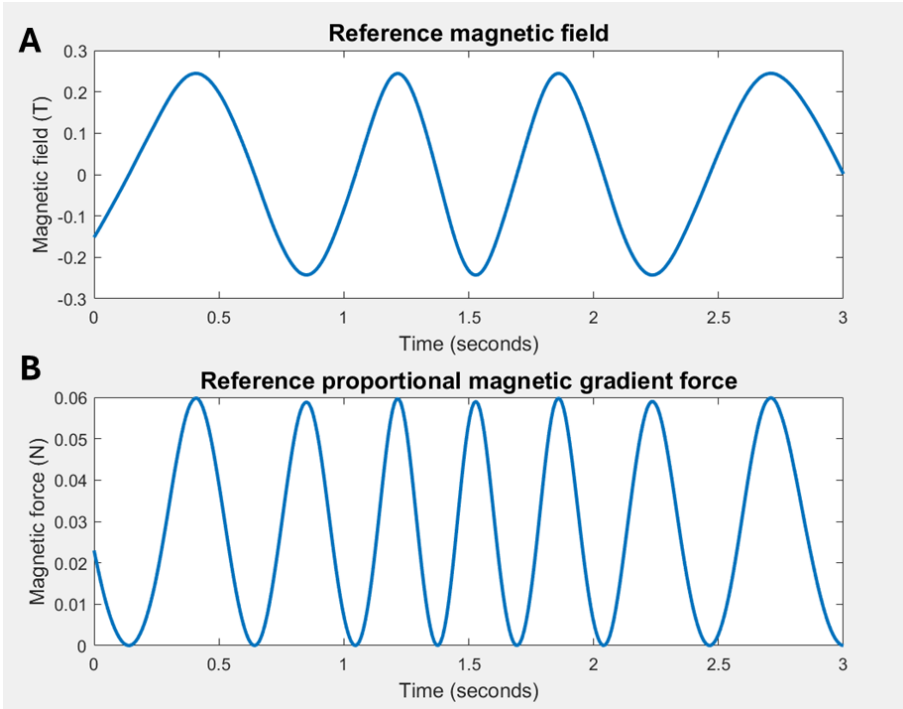

Figure 4. (A) Measured magnetic field and (B) the calculated proportional magnetic gradient force from this field. The intended duration of bidirectional chirp was 2 seconds. The force frequency spanned from 1.7 to 3.3 Hz.

For the comparison between fixed frequency versus linear bidirectional chirp magnetic excitations, all reference signals were derived from permanent magnet measurements. For fixed-frequency references, a duration of 1.5 seconds was chosen. The reference lengths for the chirped signals were scaled according to their sweep durations. A 1.5 second reference was used for the 1 second bidirectional chirps, while a 2 second reference was applied to the 2 second chirps. The extended 1.5 second window for the fast chirp was necessary to capture a complete bidirectional chirp cycle, compensating for motor lag that extended the modulation beyond its expected duration. Conversely, the 2 second reference for the slow chirp did not encompass a full frequency cycle. Instead, this duration was determined in retrospect, informed by the properties of the measured data.

3.4 Matched filter

To evaluate the probability that a pixel in the acquired ultrasound image represented a region with accumulated magnetic contrast agent, I developed a matched filter algorithm. Matched filtering was used to find similarities between the shape of the reference signal and the received signal. The filter can be performed in the time or frequency domain. In this study, the filter was performed in the frequency domain to reduce computational complexity and time.

The impulse response of a matched filter $h(t)$ in the time domain is a complex conjugate and time-reversal of the reference signal $s(t)$, see Equation (8) (Spooner et al. 2009).

$$h(t) = s^*(-t) \tag{8}$$

The impulse response was converted into the frequency domain using the fast Fourier transform (FFT). The FFT of $s(-t)$ is $S(-\omega)$ and the FFT of $s^*(t)$ is $S^*(-\omega)$ (Spanne 1995). By combining these, the resulting impulse response was defined as in Equation (9).

$$H(\omega) = S^*(\omega) \tag{9}$$

To apply the filter to a received signal $x(t)$, it was also transformed to the frequency domain with FFT to $X(\omega)$ and multiplied with the impulse response, see Equation (10).

$$Y(\omega) = X(\omega) \cdot H(\omega) = X(\omega) \cdot S^*(\omega) \tag{10}$$

With this operation, the matched filter suppressed uncorrelated components through spectral weighting. Frequencies present in the received signal but not in the reference were assigned near-zero coefficients during multiplication. The resulting output, $Y(\omega)$, was transformed back into the temporal domain using the inverse fast Fourier transform (IFFT). The amplitude in the time domain provided a direct measure of the correlation between the received signal and the reference, based on constructive interference.

The matched filter algorithm was designed in (The MathWorks Inc., USA). The RF-data were exported from the ultrasound system for analysis, where the first step was to convert all frames to I/Q data. This was done with a Hilbert transform. From the Hilbert transformation, the phase of each

pixel was retrieved over all frames in the cine-loop. The phase dimension was unwrapped to restore the continuous phase signal. The matched filter was applied on a region of interest (ROI) of the image that included the magnetic insert.

The matched filter was based on the proportional magnetic gradient force reference. The filter was applied to the phase data extracted from every pixel in the ROI across the entire frame sequence (200 or 250 frames). Before applying the matched filter, the mean was subtracted from the reference signal and phase data to center them around 0 and the phase data were detrended to mitigate drifting amplitudes. To perform matched filtering, both signals were transformed into the frequency domain using FFT before multiplying the complex conjugate of the reference with the pixel phase signal. The filtered signal was converted back to the time domain using IFFT.

Figure 5 shows an example of the phase data for a pixel in the magnetic insert region overlaid with the reference, at the point of maximum correlation between the phase data and the reference. The figure exemplifies a pixel with a high correlation with the reference. A normalized value of the correlation was calculated and the maximum absolute value of the correlation across all frames was saved. Thus, each pixel was assigned a value between 0 and 1, where 0 is a perfect mismatch and 1 is a perfect match between the phase data and the reference. The absolute value includes both matches in and out of phase with the reference, deliberately done due to unknown magnet position and phase at image initialization. The maximum correlation value for each pixel was saved in a detection image that visualized the probability of MNP presence.

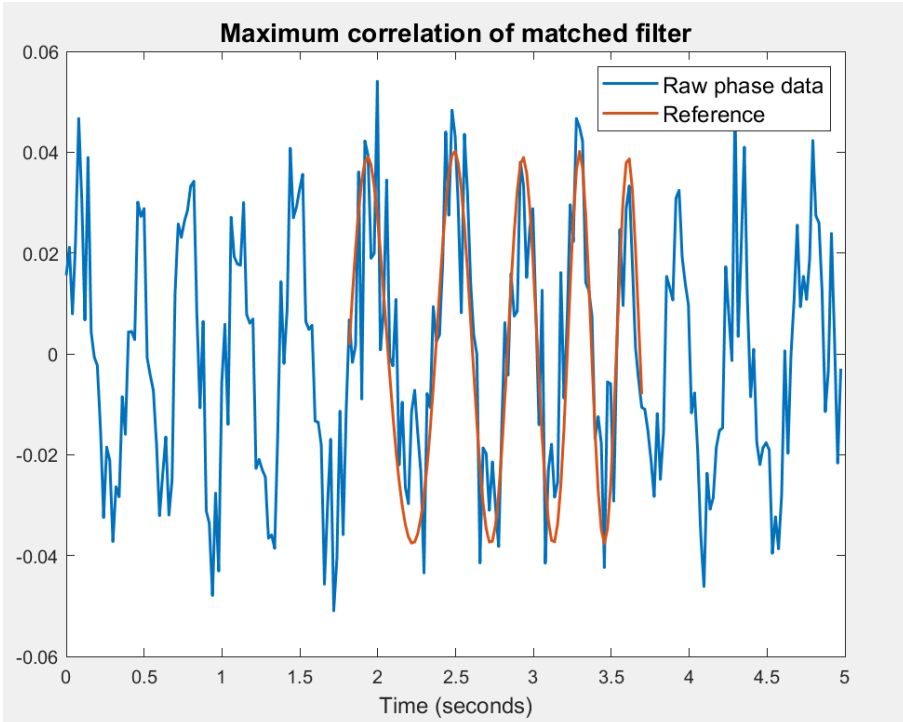

Figure 5. The reference magnetic force overlaid the phase data for a pixel in the magnetic insert region of a phantom at the point of maximum correlation. The phantom in the example had MNP concentration of 0.5 mg/ml and the excitation signal for MMUS was a bidirectional chirp with frequency span from 1.7 to 3.3 Hz with a duration of 2 seconds.

3.5 Image processing

3.5.1 Masking

In image processing, a mask is applied to an image to weight the pixel values. The values of a mask are normalized, often as a binary distribution to turn pixel values on or off.

The normalized correlation maps from the matched filter algorithm represented the likelihood of MNP presence in each pixel. With this in mind, I employed the resulting correlation as a non-binary probability mask on the displacement detection images from the previous phase tracking algorithm. This integration was a multiplication of the two algorithm results.

To take advantage of the full length of the fixed frequency MMUS images (200 frames) for masking, a 190 frame long artificial reference signal was created for the fixed 6.7 Hz frequency excitation. This was the evaluated excitation signal for the matched filter detection as a mask for the displacement detection.

3.5.2 Segmentation and morphology

Image segmentation is the process of dividing an image into separate objects or segments. One common application is to separate an image into a foreground and a background by creating a binary image parted at a specific threshold. Then, if a pixel value is lower than the threshold, it is considered as the background, and if it is larger than the threshold, it is considered as an object pixel, creating a binary mask for the image. In this contribution, segmentation was performed to separate regions of accumulated contrast agent from the background. Segmentation was performed on the detection images from the matched filter algorithm with pixel values corresponding to the maximum correlation between the phase of the pixel and the magnetic force reference.

3.5.2.1 Triangle algorithm

There are different automated algorithms for thresholding an image. An example used in this study is the "triangle algorithm" described by Zack et al. (1977). This method is suitable for thresholding an image where, if all pixels are arranged in a histogram, the values are distributed in one main peak with a tail. Figure 6 shows a pixel histogram of a detection image. The x-axis corresponds to the correlation value ranging from 0 to 1 and the y-axis is the number of pixels for each value. The threshold was determined by calculating the perpendicular distance from each bar in the histogram to the line going through the peak and tail of the histogram. The threshold was chosen as the point where this distance was maximized. In the description of the algorithm by Zack et al. (1977), a fixed offset was added to push the threshold further from the peak. This was an appropriate step in their implementation, informed by their specific test data. However, the step was not deemed relevant for this implementation and therefore excluded.

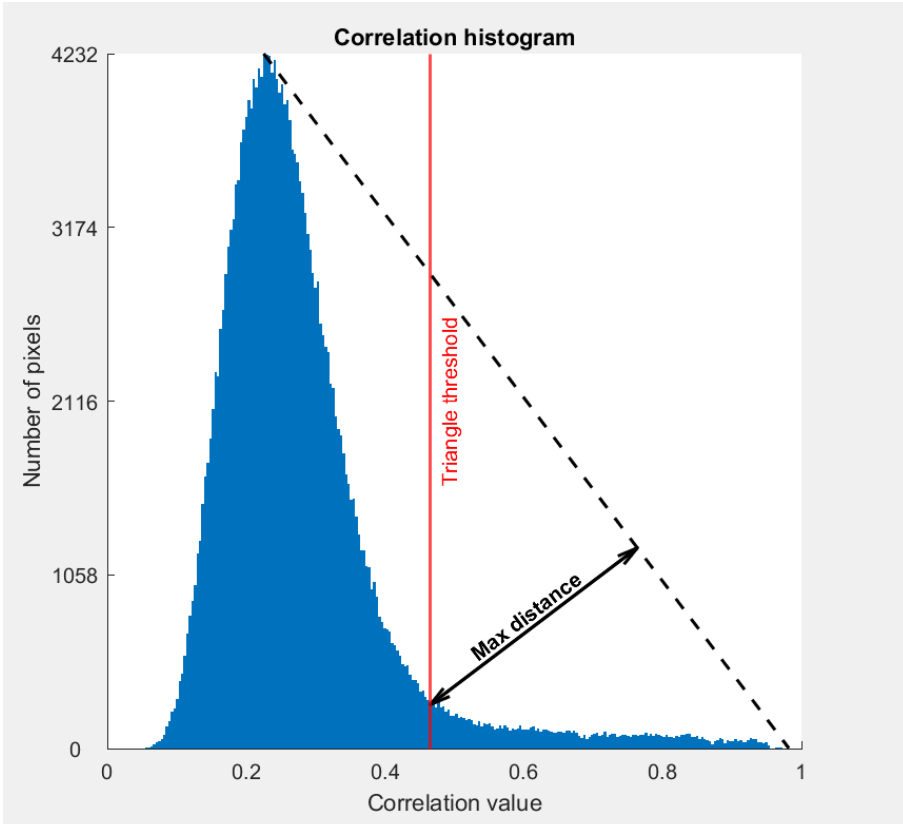

Figure 6. Visualization of how the triangle threshold was determined. The threshold was chosen as the point in the correlation histogram with a maximized perpendicular distance from the line going through the histogram peak and tail.

3.5.2.2 Otsu's method

Another thresholding algorithm is Otsu's method, described by Otsu (1979). This algorithm chooses the threshold of a normalized image as the value that minimizes the intraclass variance of the pixels in each segment when sorted into a histogram. This method was also applied to the normalized detection images from the matched filter to create a binary mask to separate the MNP regions from the background.

3.5.2.3 Additional image processing

I implemented additional image processing steps on the binary masks to achieve a clearer spatial mapping of the MNPs. To reduce noise, all foreground segments smaller than 10 pixels were removed. These were considered noise, as their high correlation values with the magnetic force ref-

erence were attributed to the random nature of noise rather than as signal. To achieve a smoother object boundary, morphological image processing steps were applied using a filter of alternating erosion and dilation. Specifically, the MatLab functions "imclose" and "imopen" were implemented using a disk-shaped structuring element with a 5-pixel radius. This element defined a neighborhood of pixels that slid over the image. During dilation, a pixel is set to 1 if any pixel within its neighborhood is 1, effectively filling small gaps. Conversely, erosion sets a pixel to 0 if any neighbor is 0, which strips away thin protrusions. By performing a closing (dilation followed by erosion) followed by an opening (erosion followed by dilation), the filter eliminated internal holes and smoothed the external boundary of the mask by removing small irregularities and noise.

3.6 Contrast-to-noise ratio

An established method to quantitatively evaluate the visibility of an object in an image compared to the background signal is a contrast-to-noise ratio (CNR). The CNR was calculated as in Equation (11),

$$CNR = \frac{\mu_o - \mu_b}{\sigma_b} \tag{11}$$

where μ_o is the mean signal of the object, μ_b is the mean signal of the background and σ_b is the standard deviation in the background signal. The object was the magnetic insert in the phantom. The CNR was converted into dB with the formula in Equation (12).

$$CNR_{dB} = 20log_{10}(CNR) \tag{12}$$

The improvements in noise suppression when using frequency modulated excitation signals and with a probability mask from matched filter detection were quantified with CNR_{dB}.

4 Results

4.1 Frequency modulated magnetic excitation

To evaluate the visibility of the magnetic insert after applying the matched filter to RF-data from the SEBS phantoms, the CNR was calculated. Examples of detection images from the matched filter are shown in Figure 7. The magnetic excitation signal for MMUS in the example was a bidirectional chirp with frequency span from 1.7 to 3.3 Hz and a duration of 2 seconds. The images show the normalized correlation from the matched filter algorithm, where the yellow color represents a perfect match (1) and the dark blue color represents a perfect mismatch (0) between the proportional magnetic force reference and the pixel phase data. The background region and the object region for CNR calculations are visualized.

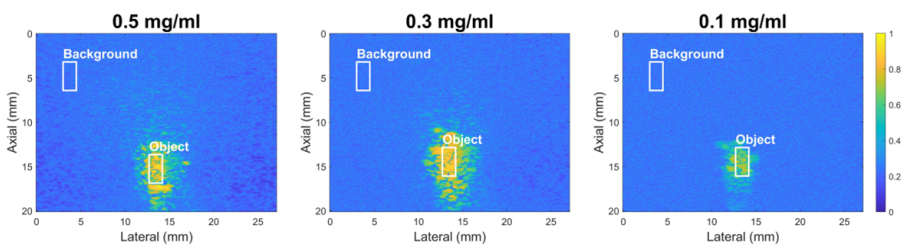

Figure 7. Normalized correlation from matched filter algorithm for MNP concentrations 0.5, 0.3 and 0.1 mg/ml in SEBS phantoms. Excitation signal for MMUS was a bidirectional chirp with frequency span from 1.7 to 3.3 Hz and a duration of 2 seconds.

The calculated mean CNR in dB for all magnetic excitation signals and for all MNP concentrations are presented in Table 1. The first three rows are fixed frequency signals and the last six are chirp signals, defined by their frequency span and duration of bidirectional frequency sweep. The mean CNR is calculated from three cross sections of each phantom. All measured CNR are presented in Appendix A, where the mean is calculated by excluding outliers. The magnetic excitation signals with the highest CNR were the linear bidirectional chirps with a duration of 2 seconds. For MNP concentrations of 0.5 and 0.3 mg/ml, the increase was approximately 2 dB compared to the fixed frequency signals and the chirps with a duration of 1 second. For MNP concentration of 0.1 mg/ml, no general improvement was observed between the excitation signals.

Table 1. Mean CNR of matched filter detection in SEBS phantoms.

Excitation signal	0.5 mg/ml	0.3 mg/ml	0.1 mg/ml
Fixed 1.7 Hz	18.06 dB	18.14 dB	15.20 dB
Fixed 6.7 Hz	18.48 dB	18.38 dB	14.44 dB
Fixed 13.3 Hz	18.52 dB	17.72 dB	11.24 dB
1.7 to 3.3 Hz, 1 s	18.30 dB	18.54 dB	13.76 dB
1.7 to 6.7 Hz, 1 s	18.38 dB	19.14 dB	13.70 dB
1.7 to 13.3 Hz, 1 s	17.74 dB	17.34 dB	12.72 dB
1.7 to 3.3 Hz, 2 s	20.52 dB	20.68 dB	14.74 dB
1.7 to 6.7 Hz, 2 s	20.06 dB	20.10 dB	11.24 dB
1.7 to 13.3 Hz, 2 s	19.52 dB	20.48 dB	14.84 dB

In Figure 8, the B-mode image of the SEBS phantom with 0.3 mg/ml MNPs is presented together with the correlation detection images from a fixed 6.7 Hz excitation and a chirp excitation with a frequency span from 1.7 to 6.7 Hz and a duration of 2 seconds. The example showcases the small visual difference of a 2 dB increase in CNR.

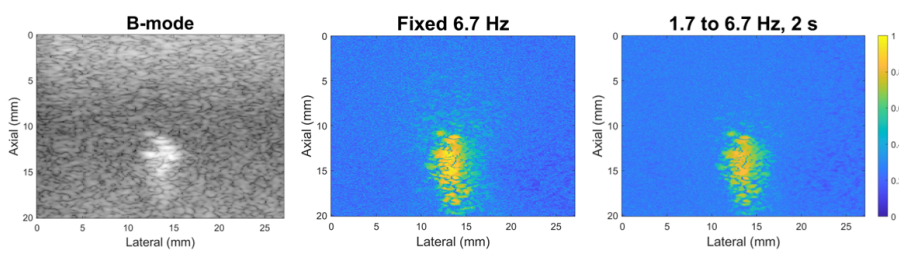

Figure 8. B-mode image together with correlation detection images from a fixed 6.7 Hz frequency excitation and a chirp excitation with frequency span from 1.7 to 6.7 Hz and a duration of 2 seconds in SEBS phantom with 0.3 mg/ml MNPs.

4.1.1 Noise

During early data analysis, it was noticed that the experiments suffered from noise at a specific frequency, 16 Hz. In Figure 9, examples of the magnitude spectrum from the first cross section of the SEBS phantom with an MNP concentration of 0.5 mg/ml are shown. Figure 9A is from

a bidirectional chirp excitation with frequency sweep from 1.7 to 3.3 Hz and 2 seconds duration, and Figure 9B is from a bidirectional chirp excitation with frequency sweep from 1.7 to 13.3 Hz and 1 second duration. The magnetic excitation signal in Figure 9A gave a CNR of 20.3 dB, while the signal in Figure 9B gave a CNR of 4.1 dB. The low CNR in B was considered an outlier in Appendix A, since the behavior was not consistent for all measurements with that excitation signal.

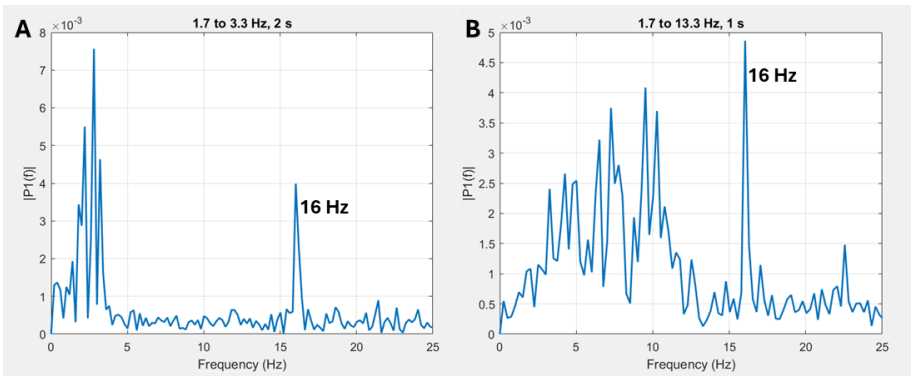

Figure 9. Single-sided magnitude spectrum derived from the FFT of the phase signal in a pixel in the magnetic insert region. Measurements from the first cross section of the SEBS phantom with MNP concentration 0.5 mg/ml. Magnetic excitation signal was a bidirectional chirp with (A) frequency sweep from 1.7 to 3.3 Hz with 2 seconds duration and (B) frequency sweep from 1.7 to 13.3 Hz with 1 second duration.

4.2 Matched filter with phase tracking algorithm

For the purpose of using the matched filter as a probability mask on the displacement detection from the previous phase tracking algorithm (Evertsson et al. 2013), a longer artificial reference was used. The reference length was 190 frames, compared to 75 frames used for the evaluation of frequency modulated excitations. Figure 10 demonstrates the detection difference between using a shorter versus a longer reference. The CNR improvement in this case, calculated with object and background boxes of the same size, was 3.4 dB. The example in Figure 10 is from the fixed 6.7 Hz excitation in a SEBS phantom with 0.3 mg/ml of MNPs.

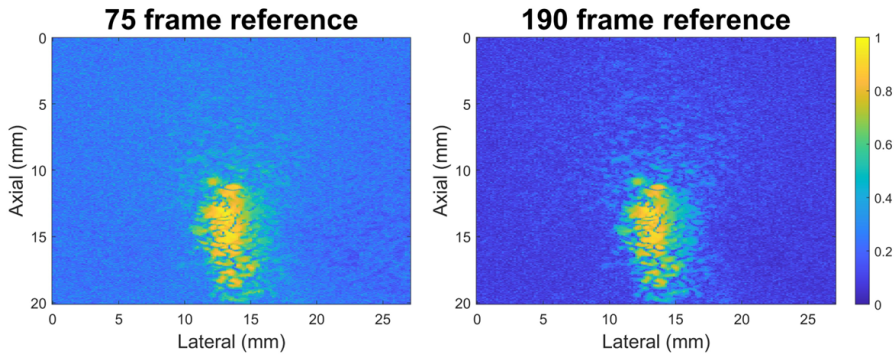

Figure 10. Comparison of the same MMUS data from a fixed 6.7 Hz excitation, matched with either a 75 frame long measured reference or a 190 frame long artificial reference. SEBS phantom with 0.3 mg/ml of MNPs.

When applying the matched filter detection as a mask for the displacement detection, noise suppression was increased. The previous detection method based on phase tracking, shown in Figure 11A, poorly defined the MNP insert region while quantitatively assessing displacement. When combined with the non-binary probability mask from the matched filter algorithm, noise suppression and boundary definition were enhanced without compromising the quantitative integrity, see Figure 11B. Both the phase tracking and the matched filter analysis in Figure 11 utilize the same MMUS data from a fixed 6.7 Hz magnetic excitation. The example in Figure 11 is of a SEBS phantom with 0.3 mg/ml of MNPs. See Appendix B for examples of 0.5 and 0.1 mg/ml of MNPs.

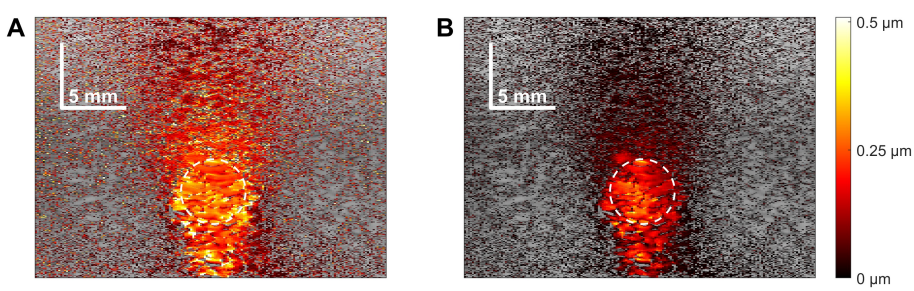

Figure 11. (A) Phase tracking algorithm detection with (B) non-binary matched filter mask overlaid the B-mode image. SEBS phantom with 0.3 mg/ml MNPs.

The improvements in noise suppression were quantified with the CNR. The mean CNR of three cross sections in SEBS phantoms with 0.5, 0.3 and 0.1 mg/ml MNPs is presented in Table 2. See Appendix C for the

full CNR calculations of all cross sections. The CNR was calculated by comparing the signal from the MNP insert (indicated by a dashed circle in Figure 11) with the surrounding.

Table 2. Mean CNR of phase tracking algorithm by itself and with the non-binary matched filter mask for a fixed 6.7 Hz MMUS excitation.

Algorithm	**0.5 mg/ml**	**0.3 mg/ml**	**0.1 mg/ml**
Phase tracking	7.33 dB	5.55 dB	-8.65 dB
Phase tracking with matched filter mask	13.91 dB	13.18 dB	4.59 dB

4.3 Image processing

When implementing the image processing steps of segmentation and morphology on the matched filter probability mask, noise suppression and boundary definition improved further. Figure 12A shows the phase tracking algorithm by itself, multiplied by the matched filter detection and segmented with either the triangle threshold (Figure 12B) or the Otsu threshold (Figure 12C). Regardless of the method chosen for thresholding, morphology filtering was implemented on the binary mask. Both the phase tracking and the matched filter analysis in Figure 12 utilize the same MMUS data from a fixed 6.7 Hz magnetic excitation. The example in Figure 12 is of a SEBS phantom with 0.3 mg/ml of MNPs. See Appendix B for examples of 0.5 and 0.1 mg/ml of MNPs.

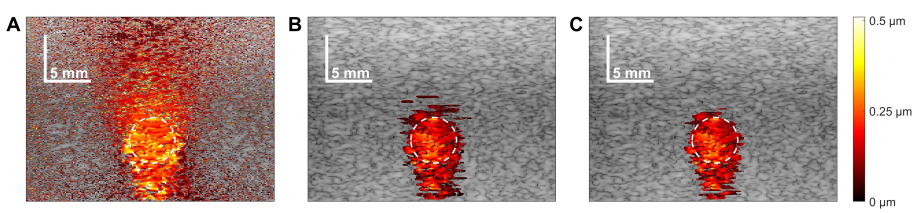

Figure 12. (A) Phase tracking algorithm detection with (B) segmented binary matched filter mask from triangle thresholding and (C) Otsu thresholding overlaid the B-mode image. SEBS phantom with 0.3 mg/ml MNPs.

The improvements in noise suppression were quantified with the CNR. The mean CNR of three cross sections in SEBS phantoms with 0.5, 0.3 and 0.1 mg/ml MNPs is presented in Table 3. See Appendix C for the

full CNR calculations of all cross sections. The CNR was calculated by comparing the signal from the MNP insert (indicated by a dashed circle in Figure 12) with the surrounding. The CNR calculations were performed on the results from the triangle mask and the Otsu mask.

Table 3. Mean CNR of phase tracking algorithm by itself and with the binary matched filter mask for a fixed 6.7 Hz MMUS excitation. Thresholding performed with the triangle or Otsu method.

Algorithm	**0.5 mg/ml**	**0.3 mg/ml**	**0.1 mg/ml**
Phase tracking	7.33 dB	5.55 dB	-8.65 dB
Phase tracking with triangle mask	14.95 dB	14.44 dB	20.58 dB
Phase tracking with Otsu mask	15.46 dB	14.89 dB	16.45 dB

4.4 PVA phantoms

The acoustic properties of the bulk and insert material in the PVA phantoms were successfully matched, as evidenced by the homogeneity of the B-mode image in Figure 13A. However, the preparation of the phantoms was compromised, rendering the resulting phantoms unsuitable for further analysis. The PVA did not fully dissolve in the water during heating, resulting in a non-uniform material with a lower viscosity than expected. Additionally, the MNP solution appeared to separate from the PVA mixture during the freeze-thaw cycles in the syringes.

The detection of the matched filter algorithm had a less defined boundary between the bulk and insert material than the phantoms with SEBS as the bulk material, see Figure 13B. However, no CNR calculations were performed for the PVA phantoms. This was prompted by the inability to distinguish the insert in the B-mode image, making an ROI decision for the CNR calculation more arbitrary. Additionally, PVA phantom preparation errors further motivated the decision to shift the focus away from them in this study.

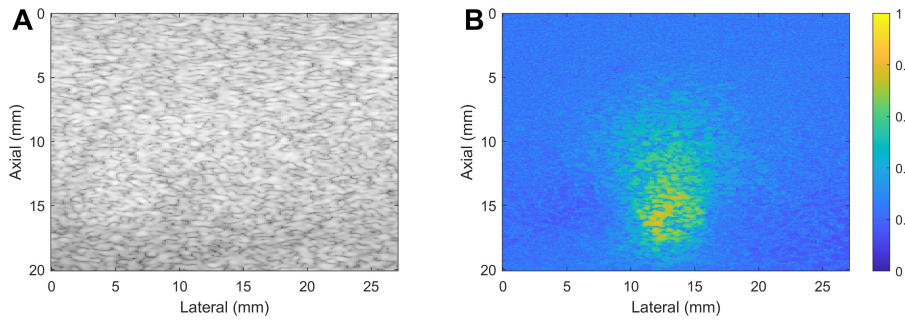

Figure 13. (A) B-mode image and (B) detection of the matched filter of the PVA phantom with 0.5 mg/ml of MNPs. The excitation signal for MMUS was a bidirectional chirp with frequency span from 1.7 to 3.3 Hz and a 2 seconds duration.

5 Discussion

5.1 Phantom material

The correlation of the matched filter in the PVA phantoms was less spatially specific than in the SEBS phantoms. Additionally, errors occurred during the preparation of the PVA phantoms. Consequently, the focus pivoted towards the SEBS phantoms for the mask and segmentation results. A probable cause for the reduced specificity in the PVA phantoms is the fact that they had the same bulk and insert material. With this configuration, it is more likely that the displacement from the MNPs is propagated faster and further in the surrounding material, making it harder to distinguish between MNP displacements and delayed responses to this displacement.

Nevertheless, PVA phantoms could be a promising topic for future investigation because PVA is a water-based material, just as human tissue. To mitigate the effects of propagating tissue displacements, my suggestion is to implement a reference between the magnet's position and phase, and image initialization. With this reference, correlations could be discriminated based on the temporal relation with the magnetic excitation. If a correlation happens with a large time delay after the excitation, it is probable that this effect comes from propagated movement through the tissue, not necessarily close to the MNPs which should move relatively soon to the magnet rotation. Successful experiments on PVA phantoms would validate the method's ability to distinguish accumulated MNPs in tissue regions that are indistinguishable in acoustic properties.

In the SEBS phantoms, the acoustic properties of the bulk material and the insert material were not the same. SEBS is an oil-based material compared to PVA. Furthermore, the graphite concentration was higher in the insert. Despite this, the use of SEBS phantoms is not unsupported. Mousavi et al. (2025) claims this kind of phantom to be acoustically close to lymph nodes in fat, which is a relevant scenario for MMUS imaging.

5.2 Region definition for CNR calculations

CNR calculations were conducted both to evaluate frequency modulated magnetic excitations and to quantify the noise suppression improvements when applying the matched filter as a mask on displacement detections.

It is worth noting that the region definition in both cases lacked ground truth. For the first case, equally large background and objects were chosen and the object region was placed arbitrarily in the region of highest correlation. For the second case, the object region was defined as a 5 mm diameter circle and the background as the surrounding. The circle was placed based on attributes in the corresponding B-mode image and on prior knowledge of the phantom construction. If a ground truth for the location of the MNPs can be obtained, the accuracy of the boundary definition can be evaluated more precisely.

5.3 Frequency modulated magnetic excitation

The results from the comparison between fixed frequency and linear bidirectional chirp magnetic excitation signals suggest that longer chirped signals provide superior noise suppression to the fixed frequency signals. However, the necessity of this relatively small improvement is questionable. A chirped signal with a longer sweep duration results in longer image acquisitions. This is incompatible for clinical applications, where image acquisitions should be as short as possible to reduce the risk of noise from patient movements, operator movements and biological functions. Furthermore, if the matched filter detection is to be combined with the phase tracking algorithm to preserve the quantitative integrity, the use of a chirped signal adds a step to the data acquisition. Since the phase tracking algorithm uses a fixed frequency excitation for analysis, it would be preferable to use the same data for matched filter analysis and segmentation. This was the reason for pivoting towards fixed frequency signals when using the matched filter as a probability mask for the phase tracking algorithm and when applying segmentation to the mask.

Moreover, the increased CNR for the 2 second duration chirps could be attributed to the length of the reference. It should be kept in mind that the reference length for the 2 seconds duration chirps was 100 frames (2 seconds), while the reference for fixed frequency and shorter chirp signals was 75 frames (1.5 seconds). The significance of this difference has not been quantified, but is a probable cause of increased CNR. The references were kept this length to give the longer chirp signals an advantage for having a larger time-bandwidth product and because the cine-loops were longer during image acquisition of these excitations.

5.3.1 Noise

Different excitation signals showed varying levels of sensitivity to the 16 Hz interference frequency. Figure 9 shows the magnitude spectrum for two example signals. In both cases, there is a clear amplitude peak at 16 Hz. However, for the broader frequency sweep signal, the amplitude of the interference is larger than the amplitude of the signal frequency, seemingly obstructing the matched filter algorithm from finding a large correlation with the magnetic force reference. All outliers in Appendix A included the 13.3 Hz frequency, suggesting that these excitation signals were more susceptible to the interference frequency. Additionally, most of the outliers were chirped excitation signals. This result contradicts the hypothesis that the implementation of frequency modulated excitation signals would increase the robustness to noise.

Several interventions were suggested and tested to reduce the interference at 16 Hz. The approaches included turning off all other motors and computers in the room with the experimental setup, placing the phantom on a foam mat, placing a weight on the phantom, moving the motor that drove the magnet to a separate table from the phantom, turning off the magnet driving motor, changing the length of the lever for the ultrasound transducer and wrapping the transducer cable in fabric. The purpose of every change was to reduce the risk of mechanical vibrations in the setup. However, no change mitigated the interference frequency. I have no clear hypothesis of what caused the interference. If the interference frequency was caused by vibrations from the ultrasound machine or transducer, it can be expected in future measurements. In this case, frequency sweeps with a larger bandwidth seem to be more sensitive and should be avoided. To rule out an external source in the local environment as the cause of the interference, I suggest that the measurements be replicated with the same setup in a second laboratory room.

5.4 Matched filter as probability mask

5.4.1 Excitation signal and reference length selection

As mentioned before, the focus pivoted towards a fixed frequency excitation for the application of matched filter as a probability mask, reasoned by the phase tracking algorithm's need for this type of excitation. Using different excitation signals for these steps does not justify the longer im-

age acquisition time and system complexity. My choice to investigate the 6.7 Hz excitation signal was reasoned by the limited number of cycles in a 4 second ultrasound cine-loop with a 1.7 Hz excitation and the 13.3 Hz excitation's sensitivity to the interference frequency at 16 Hz. Additionally, all fixed frequency signals performed similarly (Table 1), making an analysis of every frequency redundant.

The reference length was increased for the purpose of using the matched filter detection as a mask. This adjustment predictably improved noise suppression and CNR, as shorter references are more prone to correlation with noise. Consequently, a reference length approaching the total image length is more effective, clearly demonstrated by Figure 10. However, a shorter reference was used when comparing fixed frequency versus chirped excitations to ensure a fair comparison. Chirped excitations required a longer acquisition time to ensure that a full bidirectional cycle was captured. Therefore, the reference for these excitations had to be much shorter than the full image length, thus explaining the fairness of comparing this to a shorter fixed frequency reference.

5.4.2 Mechanism and interpretation of the combined algorithm

The implementation of the matched filter as a mask for displacement detection from the previous phase tracking algorithm resulted in enhanced noise suppression and boundary definition. This improvement implies that the detection of MNPs in MMUS can be specific, likely allowing detection of lower MNP concentrations. Successfully locating small concentrations of MNPs would increase the monitoring sensitivity for drug administration, intraoperative guidance and molecular change detection. This would elevate the diagnostic and therapeutic relevance of MMUS.

To understand why the matched filter improves the noise suppression compared to when phase tracking is used by itself, it is important to note the different approaches. The phase tracking algorithm calculates the mean phase of the pixel phase from the RF-data, and a manual gate decides which phases should be kept. In this way, the pixels that move together close in time at the right frequency are kept and their displacement is calculated. Phase gating requires some prior knowledge of where the MNPs are located to make a relevant phase decision, matching the phase of the magnetic insert. In comparison, the matched filter does not

require any manual interventions. Furthermore, it does not calculate displacement and does not operate based on the phase of the pixel phase. Rather, the filter is about the shape of the phase oscillation. With the matched filter, received pixel phase signals that do not contain the spectral components of the reference template or do not match the timing and duration of the reference template result in a worse correlation. These approaches may seem similar but the phase tracking algorithm operates by mixing the received signal with quadrature demodulation of the target frequency while the matched filter filters the signal based on frequency spectrum and constructive interference. The results in this study indicate the increased detection specificity of shape matching the phase signal to a reference template over tracking the phase of the phase signal. However, the methods must be combined to avoid loss of quantitative detection.

The physical interpretation of the product of displacement detection and probability detection can be conceptually aligned with the energy transfer detection of the MNPs. This is not a perfect analogy since the probability has no unit, meaning the output still has a length unit. To make sense of the analogy, the probability is considered as the force or mass of the MNPs. In simpler, and more factual terms, the matched filter combined with the displacement detection is a weighted displacement detection. The weight is based on the probability of detected MNPs and does not scale with the concentration.

5.5 Image processing

The application of segmentation and morphological filtering on the probability mask from the matched filter detection further increased the boundary definition of MNP regions. This is exemplified by the results in Figure 12 and Appendix B. Implementing image processing is always a matter of interpreting the data, in this case to decide where contrast agents have accumulated or not. However, it is important to implement filtering techniques with caution to reduce the risk of losing MNP information caused by too strict filtering.

Two thresholding methods were compared for segmentation, the triangle and the Otsu method. For contrast agent concentrations of 0.5 and 0.3 mg/ml, the Otsu method performed better than the triangle method. At a concentration of 0.1 mg/ml MNPs, the mean CNR across the three im-

aged cross sections indicates that the triangle method had superior performance. However, the first column of Table 9 in Appendix C presents the results for a specific cross section in the SEBS phantom with 0.1 mg/ml of MNPs. The CNR results for this cross section did not follow the pattern of all other measurements. This could be considered an outlier, but it was not done in order to showcase the difficulty in identifying MNP presence at low concentrations. The lowest concentration of contrast agent yield the smallest displacements and phase shifts, evidently creating more fluctuation in the detection results. With this in mind, the triangle segmentation still increased the CNR for this particular detection by 29 dB.

5.6 Ethics discussion

During the development of any medical application, it is important to conduct animal and/or clinical studies to ensure safety and efficiency. It is an important step from discovery to clinical implementation. Clinical studies (which avoid selection bias by including a heterogeneous sample population) ensure that a method does not only work for one type of person with a specific tissue composition. However, to evaluate technical properties, the use of tissue-mimicking phantoms is often considered to have an ethical advantage over human and animal studies (Mousavi et al. 2025). This belief is built on the 3R principle first introduced by Russell et al. (1959). The 3R terms are replace, reduce and refine. These principles were formulated specifically with the ethics surrounding animal research in mind to reduce suffering and save animal studies for clinical investigations. Considering this, it is ethically justifiable that this study was performed on phantoms.

When developing new technology for medical applications, equality is a major ethical consideration. The ultimate scenario is that technology becomes available and beneficial to all people, regardless of their social and economic status. The development of MMUS, a molecular specific imaging modality based on ultrasound, is aimed at achieving this equality. Ultrasound is one of the most widely used imaging modality for medical applications with a lower cost than other techniques (Hoskins et al. 2019). This makes MMUS a relatively available technique, reducing the need for large machines such as MRI and PET scanners, while providing the molecular specificity of these techniques, with the aim of improving healthcare quality globally.

6 Conclusion

By using a linear bidirectional chirped magnetic excitation for MMUS imaging, the CNR between the MNP region and the background is slightly increased compared to when using a fixed frequency excitation. However, this small improvement does not justify the longer image acquisition time and system complexity, especially when combined with the previous phase tracking algorithm that needs a fixed frequency excitation. Additionally, frequency modulated signals were most susceptible to the interference frequency during experiments, contradicting the hypothesis that these excitations would increase robustness to noise.

The matched filter algorithm described in this study is an efficient strategy for noise suppression and spatial specificity in MMUS imaging. When image processing steps are included, the efficiency is enhanced further. By combining the matched filtering with the previous detection method, the quantitative displacement analysis is retained. Decreasing the detection limit of MNPs for MMUS with these strategies could increase the diagnostic and therapeutic capacity of the technique.

References

Eugenio (2026). *Commanding Maxon Motors EPOS2 Motor Controller from MATLAB*. Version 2.0.

Evertsson, Maria, Magnus Cinthio, Sarah Fredriksson, Fredrik Olsson, Hans W. Persson, and Tomas Jansson (2013). "Frequency- and phase-sensitive magnetomotive ultrasound imaging of superparamagnetic iron oxide nanoparticles". In: *IEEE Transactions on Ultrasonics, Ferroelectrics and Frequency Control* 60.3, pp. 481–491. DOI: 10.1109/TUFFC.2013.2591.

Evertsson, Maria, Pontus Kjellman, Magnus Cinthio, Roger Andersson, Thuy A Tran, Rene In'T Zandt, Gustav Grafström, Hanna Toftevall, Sarah Fredriksson, Christian Ingvar, Sven-Erik Strand, and Tomas Jansson (2017). "Combined Magnetomotive ultrasound, PET/CT, and MR imaging of 68Ga-labelled superparamagnetic iron oxide nanoparticles in rat sentinel lymph nodes in vivo". In: *Scientific Reports* 7.1, p. 4824. DOI: 10.1038/s41598-017-04396-z.

Fink, Michael, Helmut Ermert, Christoph Alexiou, and Stefan Lyer (2017). "C2.2 - Detection of Iron Oxide Nanoparticles for Local Chemotherapeutic Treatment Employing Coded Magnetomotive Ultrasound". In: *Proceedings Sensor 2017*. AMA Conferences 2017. Nürnberg, Germany: AMA Service GmbH, Von-Münchhausen-Str. 49, 31515 Wunstorf, Germany, pp. 323–328. DOI: 10.5162/sensor2017/C2.2.

Fink, Michael, Helmut Ermert, Stefan Lyer, and Christoph Alexiou (2016). "Sonographic detection of magnetic nanoparticles for Magnetic Drug Targeting using coded magnetic fields". In: *2016 IEEE International Ultrasonics Symposium (IUS)*. 2016 IEEE International Ultrasonics Symposium (IUS). Tours, France: IEEE, pp. 1–6. DOI: 10.1109/ULTSYM.2016.7728404.

Gu, Yaning, Han Zheng, Wenhao Zhong, Gaixia Xu, Mian Chen, Haoming Lin, Siping Chen, and Xin Chen (2025). "Sensitivity-Boosted Magnetomotive Ultrasound Imaging via Electromagnetic-Coded Excitation". In: *2025 IEEE International Ultrasonics Symposium (IUS)*. 2025 IEEE International Ultrasonics Symposium (IUS). Utrecht, Netherlands: IEEE, pp. 1–4. DOI: 10.1109/IUS62464.2025.11201688.

Hood, Leroy, James R. Heath, Michael E. Phelps, and Biaoyang Lin (2004). "Systems Biology and New Technologies Enable Predictive and Preventative Medicine". In: *Science* 306.5696, pp. 640–643. DOI: 10.1126/science.1104635.

Hoskins, Peter, Kevin Martin, and Abigail Thrush (2019). *Diagnostic Ultrasound, Third Edition*. 3rd ed. Physics and Equipment. CRC Press. DOI: 10.1201/9781138893603.

Hussain, Shah, Iqra Mubeen, Niamat Ullah, Syed Shahab Ud Din Shah, Bakhtawar Abduljalil Khan, Muhammad Zahoor, Riaz Ullah, Farhat Ali Khan, and Mujeeb A. Sultan (2022). "Modern Diagnostic Imaging Technique Applications and Risk Factors in the Medical Field: A Review". In: *BioMed Research International* 2022.1. Ed. by Chen Li, p. 5164970. DOI: 10.1155/2022/5164970.

Mousavi, Arefeh, Jules Reniaud, Magnus Santesson, Linda Persson, and Tomas Jansson (2025). "Design of a Phantom Mimicking Rectal Lymph Nodes for Magnetomotive Ultrasound". In: *Ultrasound in Medicine & Biology* 51.1, pp. 77–84. DOI: 10.1016/j.ultrasmedbio.2024.09.010.

O'Donnell, Matthew (2018). "Magnetic nanoparticles as contrast agents for molecular imaging in medicine". In: *Physica C: Superconductivity and its Applications* 548, pp. 103–106. DOI: 10.1016/j.physc.2018.02.031.

Otsu, Nobuyuki (1979). "A Threshold Selection Method from Gray-Level Histograms". In: *IEEE Transactions on Systems, Man, and Cybernetics* 9.1, pp. 62–66. DOI: 10.1109/TSMC.1979.4310076.

Russell, W.M.S and R.L Burch (1959). *The principles of humane experimental technique*. London: Methuen & Co. Ltd.

Sjöstrand, Sandra, Maria Evertsson, and Tomas Jansson (2020). "Magnetomotive Ultrasound Imaging Systems: Basic Principles and First Applications". In: *Ultrasound in Medicine & Biology* 46.10, pp. 2636–2650. DOI: 10.1016/j.ultrasmedbio.2020.06.014.

Sjöstrand, Sandra, Maria Evertsson, Ulrika Lindquist, Rebecka Lindkvist, Roger Andresson, Anders Wahlstrom, Goran Nybom, Ingrid Svensson, Magnus Cinthio, and Tomas Jansson (2018). "Revolving Permanent Magnet for Magnetomotive Ultrasound". In: *2018 IEEE International Ultrasonics Symposium (IUS)*. 2018 IEEE International Ultrasonics Symposium (IUS). Kobe: IEEE, pp. 1–3. DOI: 10.1109/ULTSYM.2018.8580041.

Spanne, Sven (1995). *Lineära system*. Vol. 3. pp. 253-256. Lund: KFS i Lund AB.

Spooner, Chad M. and Richard B. Nicholls (2009). "Spectrum Sensing Based on Spectral Correlation". In: *Cognitive Radio Technology*. El-

sevier, pp. 593–634. DOI: 10.1016/B978-0-12-374535-4.00018-7.

Zack, G.W., W.E Rogers, and S.A. Latt (1977). “Automatic measurement of sister chromatid exchange frequency.” In: *Journal of Histochemistry & Cytochemistry* 25.7, pp. 741–753. DOI: 10.1177/25.7.70454.

Appendix A

All CNR values from matched filter detection of different excitation signals for SEBS phantoms with MNP concentrations 0.5, 0.3 and 0.1 mg/ml are presented in Table 4, Table 5 and Table 6. Three cross sections (CS) were imaged for each phantom and the mean values were calculated by excluding outliers marked with red text.

Table 4. CNR in SEBS phantom with 0.5 mg/ml of MNPs for different magnetic excitation signals.

Excitation signal	CS 1	CS 2	CS 3	Mean
Fixed 1.7 Hz	18.14 dB	17.70 dB	18.32 dB	18.06 dB
Fixed 6.7 Hz	18.72 dB	18.14 dB	18.54 dB	18.48 dB
Fixed 13.3 Hz	18.42 dB	18.06 dB	19.02 dB	18.52 dB
1.7 to 3.3 Hz, 1 s	18.28 dB	17.82 dB	18.78 dB	18.30 dB
1.7 to 6.7 Hz, 1 s	17.86 dB	17.80 dB	19.38 dB	18.38 dB
1.7 to 13.3 Hz, 1 s	4.10 dB	16.40 dB	18.90 dB	17.74 dB
1.7 to 3.3 Hz, 2 s	20.28 dB	20.20 dB	21.04 dB	20.52 dB
1.7 to 6.7 Hz, 2 s	20.26 dB	19.44 dB	20.48 dB	20.06 dB
1.7 to 13.3 Hz, 2 s	17.56 dB	17.80 dB	22.30 dB	19.52 dB

Table 5. CNR in SEBS phantom with 0.3 mg/ml of MNPs for different magnetic excitation signals.

Excitation signal	CS 1	CS 2	CS 3	Mean
Fixed 1.7 Hz	18.82 dB	18.34 dB	17.20 dB	18.14 dB
Fixed 6.7 Hz	18.74 dB	18.96 dB	17.36 dB	18.38 dB
Fixed 13.3 Hz	18.98 dB	17.50 dB	16.52 dB	17.72 dB
1.7 to 3.3 Hz, 1 s	19.48 dB	18.92 dB	17.02 dB	18.54 dB
1.7 to 6.7 Hz, 1 s	19.82 dB	19.26 dB	18.26 dB	19.14 dB
1.7 to 13.3 Hz, 1 s	17.62 dB	17.04 dB	10.92 dB	17.34 dB
1.7 to 3.3 Hz, 2 s	21.30 dB	20.88 dB	19.76 dB	20.68 dB
1.7 to 6.7 Hz, 2 s	21.16 dB	20.28 dB	18.68 dB	20.10 dB
1.7 to 13.3 Hz, 2 s	20.14 dB	21.88 dB	19.20 dB	20.48 dB

Table 6. CNR in SEBS phantom with 0.1 mg/ml of MNPs for different magnetic excitation signals.

Excitation signal	CS 1	CS 2	CS 3	Mean
Fixed 1.7 Hz	10.24 dB	15.90 dB	17.82 dB	15.20 dB
Fixed 6.7 Hz	7.30 dB	14.94 dB	17.96 dB	14.44 dB
Fixed 13.3 Hz	1.62 dB	9.66 dB	12.82 dB	11.24 dB
1.7 to 3.3 Hz, 1 s	7.10 dB	15.06 dB	16.50 dB	13.76 dB
1.7 to 6.7 Hz, 1 s	6.44 dB	13.30 dB	17.82 dB	13.70 dB
1.7 to 13.3 Hz, 1 s	-4.22 dB	9.72 dB	14.94 dB	12.72 dB
1.7 to 3.3 Hz, 2 s	8.78 dB	15.64 dB	17.56 dB	14.74 dB
1.7 to 6.7 Hz, 2 s	4.50 dB	14.34 dB	12.12 dB	11.24 dB
1.7 to 13.3 Hz, 2 s	-5.22 dB	16.14 dB	13.32 dB	14.84 dB

Appendix B

Figure 14 presents a cross section of the SEBS phantom with 0.5 mg/ml of MNPs. In Figure 14A, the detection of MNPs is executed with the phase tracking algorithm, Figure 14B shows the detection when the matched filter detection is employed as a non-binary probability mask on the displacement detection and in Figure 14C, segmentation is performed with the Otsu method and morphological filtering is applied. The corresponding steps are presented in Figure 15A, Figure 15B and Figure 15C but for a cross section of the SEBS phantom with 0.1 mg/ml of MNPs.

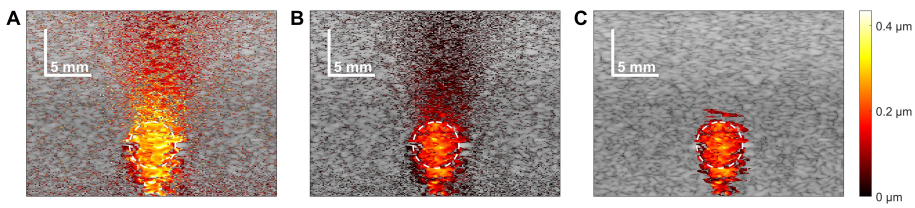

Figure 14. (A) Phase tracking algorithm detection with (B) non-binary matched filter mask and (C) binary mask from Otsu thresholding overlaid the B-mode image. SEBS phantom with 0.5 mg/ml MNPs.

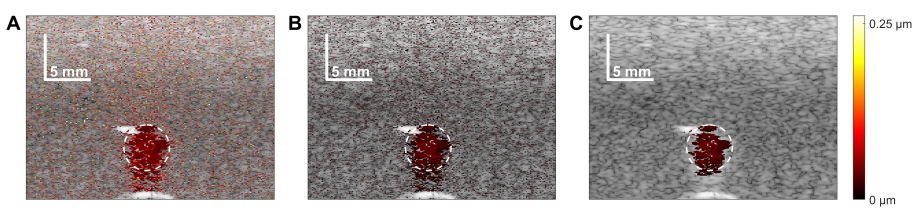

Figure 15. (A) Phase tracking algorithm detection with (B) non-binary matched filter mask and (C) binary mask from Otsu thresholding overlaid the B-mode image. SEBS phantom with 0.1 mg/ml MNPs.

Appendix C

All CNR values for SEBS phantoms with MNP concentrations 0.5, 0.3 and 0.1 mg/ml from different detection algorithms are presented in Table 7, Table 8 and Table 9. Three cross sections (CS) were imaged for each phantom.

Table 7. CNR for SEBS phantom with 0.5 mg/ml of MNPs for different detection algorithms.

Algorithm	**CS 1**	**CS 2**	**CS 3**
Phase tracking	7.31 dB	7.36 dB	7.31 dB
Phase tracking with matched filter mask	14.10 dB	14.13 dB	13.51 dB
Phase tracking with triangle mask	15.15 dB	15.34 dB	14.36 dB
Phase tracking with Otsu mask	15.81 dB	15.87 dB	14.69 dB

Table 8. CNR for SEBS phantom with 0.3 mg/ml of MNPs for different detection algorithms.

Algorithm	**CS 1**	**CS 2**	**CS 3**
Phase tracking	5.56 dB	5.46 dB	5.63 dB
Phase tracking with matched filter mask	13.59 dB	13.30 dB	12.65 dB
Phase tracking with triangle mask	14.95 dB	14.42 dB	13.95 dB
Phase tracking with Otsu mask	15.37 dB	15.06 dB	14.23 dB

Table 9. CNR for SEBS phantom with 0.1 mg/ml of MNPs for different detection algorithms.

Algorithm	**CS 1**	**CS 2**	**CS 3**
Phase tracking	-9.91 dB	-9.70 dB	-6.34 dB
Phase tracking with matched filter mask	0.05 dB	4.95 dB	8.77 dB
Phase tracking with triangle mask	19.27 dB	20.13 dB	22.31 dB
Phase tracking with Otsu mask	3.49 dB	20.25 dB	25.60 dB